UCLA

Title

A pUL25 dimer interfaces the pseudorabies virus capsid and tegument

Permalink

https://escholarship.org/uc/item/8wt5r5nj

Journal

Journal of General Virology, 98(11)

ISSN

0022-1317

Authors

Liu, Yun-Tao
Jiang, Jiansen
Bohannon, Kevin Patrick
et al.

Publication Date

2017-11-01

DOI

10.1099/jgv.0.000903

Peer reviewed

A pUL25 dimer interfaces the pseudorabies virus capsid and tegument

Yun-Tao Liu,[1,2,3]† Jiansen Jiang,[1,2]† Kevin Patrick Bohannon,[4]‡ Xinghong Dai,[1,2] G. W. Gant Luxton,[4]§ Wong Hoi Hui,[2] Guo-Qiang Bi,[3] Gregory Allan Smith[4] and Z. Hong Zhou[1,2,*]

Abstract

Inside the virions of α-herpesviruses, tegument protein pUL25 anchors the tegument to capsid vertices through direct interactions with tegument proteins pUL17 and pUL36. In addition to promoting virion assembly, both pUL25 and pUL36 are critical for intracellular microtubule-dependent capsid transport. Despite these essential roles during infection, the stoichiometry and precise organization of pUL25 and pUL36 on the capsid surface remain controversial due to the insufficient resolution of existing reconstructions from cryo-electron microscopy (cryoEM). Here, we report a three-dimensional (3D) icosahedral reconstruction of pseudorabies virus (PRV), a varicellovirus of the α-herpesvirinae subfamily, obtained by electron-counting cryoEM at 4.9 Å resolution. Our reconstruction resolves a dimer of pUL25 forming a capsid-associated tegument complex with pUL36 and pUL17 through a coiled coil helix bundle, thus correcting previous misinterpretations. A comparison between reconstructions of PRV and the γ-herpesvirus Kaposi's sarcoma-associated herpesvirus (KSHV) reinforces their similar architectures and establishes important subfamily differences in the capsid–tegument interface.

INTRODUCTION

The *Herpesviridae* family of viruses is classified into three subfamilies (α, β and γ) based on genome sequence, tissue tropism, replication cycle and pathogenicity. Human α-herpesviruses are neurotropic and include herpes simplex virus type 1 (HSV-1), herpes simplex virus type 2 (HSV-2), and varicella zoster virus (VZV). HSV-1 and HSV-2 are responsible for cold sores and genital herpes, respectively, whereas VZV causes chicken pox in children and shingles in adults [1]. Pseudorabies virus (PRV) is a veterinary α-herpesvirus that causes severe Aujeszky's disease in pigs and serves as a model for mechanistic investigations into α-herpesvirus neurotropism due to its broad host range, ease of manipulation and neuroinvasive properties [2]. Like HSV and VZV, PRV spreads from epithelial cells to innervating

sensory and autonomic neurons of the peripheral nervous system, where it establishes a persistent infection. In severe cases, HSV, VZV and PRV can spread to the central nervous system, resulting in devastating encephalitis [3–7]. Thanks to its capability of trans-synaptic spreading in the nervous system, PRV is widely used as a self-amplifying tracer for mapping neural circuits [8, 9].

Herpesviruses share a common architecture: a double-stranded DNA-containing nucleocapsid and a glycoprotein-studded lipid envelope that is separated by a poorly resolved proteinaceous tegument compartment [10, 11]. The tegument can be roughly divided into inner (capsid-proximal) and outer (envelope-proximal) layers [12–14]. Following fusion of the envelope with the host cell, the capsid and tegument are deposited into the cytosol. The outer tegument

proteins dissociate from the capsid, exposing the capsid-associated inner tegument layer [5, 15, 16], which mediates dynein-dependent capsid transport along microtubules to the nucleus [17–24]. In α-herpesvirus virions, at least a portion of the inner tegument layer interacts with the nucleocapsid in an ordered manner and presents at the icosahedral vertices [25]. Although this capsid-associated density was first interpreted as a heterodimer composed of pUL17 and pUL25 [26, 27], the largest tegument proteins pUL36 (VP1/2) were shown to be a third component, consistent with observations that an isoform of pUL36 is associated with nuclear capsids and contributes to their nuclear egress [28, 29]. Similar capsid-associated density was also observed in capsids isolated from the nuclei of infected cells, where it was termed either the C-capsid-specific component (CCSC) [27, 30] or the capsid-vertex-specific component (CVSC) [26, 29], and in γ-herpesvirus, where it was termed the capsid-associated tegument component/complex (CATC) [31]. (The CATC designation of this density is in line with the original gene annotations and functional analyses of pUL17, pUL25 and pUL36 as tegument proteins [32–35], and is chosen here to facilitate our comparison of tegument densities across subfamilies of herpesviruses.) By contrast, β-herpesviruses possess a capsid-associated tegument protein, pp150, that forms a proteinaceous net enclosing the entire capsid, presumably to buttress it against the internal pressure of their large genomes [36–40]. In both cases, CATCs are essential for virus propagation [32, 41, 42].

In an effort to better understand the capsid–tegument interface, several groups have used green fluorescence protein (GFP) as a fiducial mark to assign proteins to cryoEM densities. For example, an enhanced GFP-tagged pUL25 produced an added density on the CATC of HSV-1 and PRV [27, 43]. The position of the N-terminus of HSV-1 pUL25 was further delineated in cryoEM reconstructions by the addition of a tandem affinity purification tag [44]. Despite these important advances, the overall resolution obtained by cryoEM in these studies was insufficient to model the bulk of pUL25 accurately, let alone pUL17, within the CATC density [27]. A recently solved 6 Å reconstruction of the γ-herpesvirus KSHV allowed for the sufficient resolution of capsid structural densities, such that protein assignments could be made with high confidence [31]. This structure revealed the N-terminal segment of the KSHV pUL25 homologue, pORF19, suggesting that the assignment for pUL25 within the HSV-1 CATC may require revision [27, 43, 44], and that the level of conservation of these CATC elements between KSHV and HSV-1 should be further explored.

Another important insight into the α-herpesvirus capsid–tegument interface was provided by the recently solved 7 Å cryoEM reconstructions of HSV-1 and PRV, which clearly resolved two similarly sized globular densities in the CATCs of these viruses [45]. Consistent with KSHV, one of the globular densities was assigned to pUL25 [31]. The second density was interpreted to be a portion of pUL36; however, the lack of direct evidence clearly identifying the position of pUL36 leaves this possibility open to question. Therefore, to better understand the α-herpesvirus capsid–tegument interface it is critical that a higher resolution structure of the CATC and its associated globular densities be obtained.

Here we used a Titan Krios electron microscope equipped with a direct electron detector to image intact virions of PRV, and obtained a reconstruction at 4.9 Å resolution. Our reconstruction resolved the two globular structures of the CATC sufficiently for us to be able to assign them to belong to a pUL25 homodimer. This pUL25 homodimer organization corrects the previous interpretation of the two globular structures as a heterodimer of pUL25 and pUL36 [45]. In addition, the new reconstruction shows the detailed organization of pUL17 within the CATC and the contributions of the pUL36 tegument protein to the CATC. These refinements of the α-herpesvirus capsid–tegument interface are in general accord with the KSHV architecture, while establishing key differences in their detailed structures.

RESULTS

Overall structural organization of the PRV reconstruction

Purified PRV virions were imaged by cryoEM in the super-resolution direct electron counting mode (Fig. 1a). We obtained a three-dimensional (3D) reconstruction at a resolution of 4.9 Å by combining 13 537 virion particles and imposing an icosahedral symmetry upon them (Figs 1a, S1 and Movie S1, available in the online online Supplementary Material). The resulting PRV density map revealed the icosahedrally ordered components of the PRV virion, including the capsid (triangulation number T=16), with its characteristic structural components (12 pentons, 150 hexons and 320 triplexes; yellow to cyan in Fig. 1b and Movie S1) and 12 sets of CATC (Fig. 1b). These architectural elements are the same as those described in earlier reports of PRV at lower resolution [26, 27, 43, 45]. In agreement with our estimated resolution, striking grooves of helices can be clearly identified when the capsid structure is viewed from beneath the hexon (Fig. 1c, d). In addition, the crystal structure of the HSV-1 major capsid protein (MCP) upper domain (PDB ID: 1NO7) [46] fits precisely into the new density map (Fig. 1e and Movie S2).

Five CATC densities form star-shaped assemblies (blue in Fig. 1b) that crown each of the 12 capsid vertices. At this improved resolution, these densities are remarkably similar to the CATC described in KSHV [31]. Although it is at a slightly lower resolution than the capsid, the ~6 Å resolution of the CATC structure in our 3D reconstruction (Fig. S1) is sufficient for establishing rough molecular boundaries and for the identification of secondary structural elements such as α-helices (Fig. 1f, g). The mean density of the CATC is weaker than that of the surrounding capsid proteins. As such, the CATC can only be partially visualized when it is displayed at the same density threshold level (four times the standard deviation above the mean) as that used for
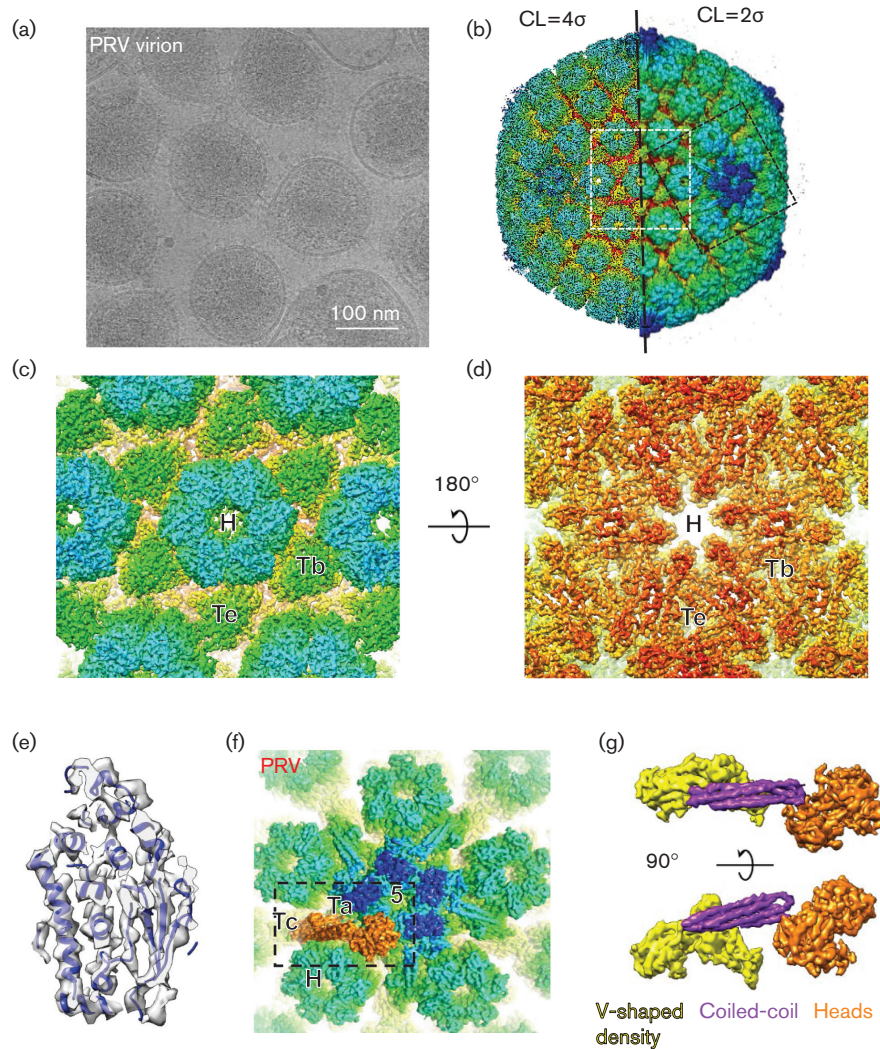
Fig. 1. CryoEM reconstruction of PRV at 4.9 Å resolution. (a) CryoEM image of PRV virions. (b) 3D reconstruction of the PRV virion at 4.9 Å, coloured radially. The left and right halves of the capsid are rendered at a contour level (CL) of four and two times standard deviations above the mean density (σ), respectively. The write box and the black dashed box demark a hexon and a vertex region containing five CATCs, respectively. (c, d) Top and bottom views of the hexon as demarked by the write box in (b). H, hexon; Tb and Te, triplexes. (e) A slab of the PRV MCP upper domain (MCPud) density map (transparent grey) fitted with the HSV-1 MCPud atomic model (blue ribbon; PDB ID: 1NO7) (f) Front view of the CATC-crowning penton as demarked by the box in (b). One of the five CATC complexes is highlighted in orange. 5, fivefold axis; Ta and Tc, triplexes; H, Hexon. (g) Two different views of the CATC containing two intertwining globular heads (orange), coiled-coil (purple) and V-shaped density (yellow).

displaying the capsid. However, the CATC subunits can be distinguished when displayed at a lower threshold level (two times the standard deviation above the mean) (Figs 1b, f and S1).

The most prominent feature of the CATC is a coiled-coil formed by a bundle of five stem helices (Fig. 1g). Attached to the vertex-proximal end of the coiled-coil are the two intertwining globular densities (or heads) that were recently observed with HSV-1 [45], while attached to the other end is an inverted V-shaped density with its two sides bridging over the two triplexes (Ta and Tc) closest to the penton (Fig. 1f, g).

In situ structure of a pUL25 dimer within the CATC

The two intertwining head densities on the vertex-proximal end of the CATC coiled-coil are similar in size and shape, suggesting that they are likely a homodimer (Fig. 2a, b and Movie S1). Indeed, the crystal structure of the truncated HSV-1 pUL25 [amino acids (aa) 130–580] [47] (PDB ID: 2F5U), referred to as the pUL25 head domain, fits perfectly within each of the two intertwining globular densities of the PRV CATC (Fig. 2c and Movie S1). We term the pUL25 subunit closer to the fivefold capsid axis the 'upper pUL25' and the other subunit the 'lower pUL25' (Fig. 2a). Further confirmation of this assignment is provided by the
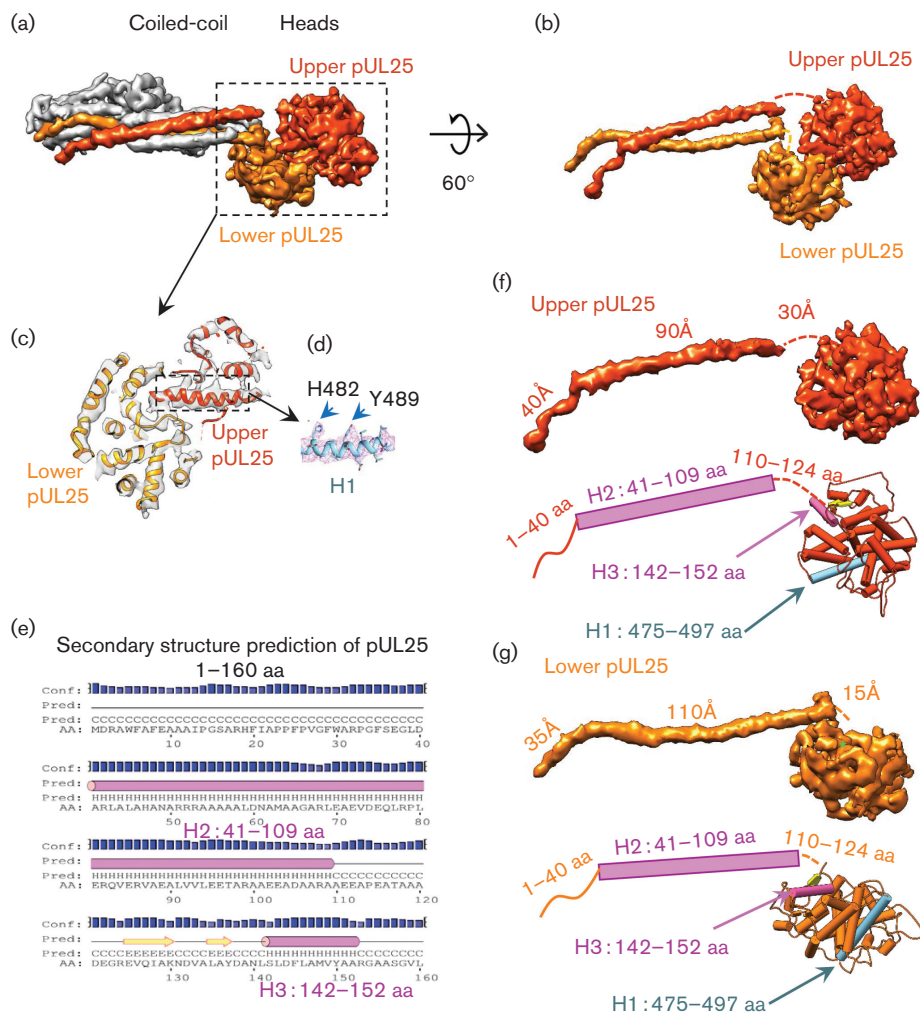
Fig. 2. Each CATC contains a dimer of pUL25. (a, b) CATC in two different views. For clarity, only densities for the pUL25 dimer are displayed in (b) to better reveal the N-terminal segments of both monomers of the pUL25 dimer. (c) One density slab of the boxed region of (a) revealing the excellent match of α-helices in the X-ray models of the HSV-1 pUL25 globular domain (ribbon) and the PRV cryoEM density map. (d) An example of bulky aromatic side-chains in the cryoEM map: aromatic side-chains H482 and Y489 of the helix (H1, 475–497 aa) of the upper monomer of the pUL25 dimer. (e) Secondary structure prediction of PRV pUL25 N-terminal domain. Two helices (H2, 41–109 aa; H3, 142–152 aa) and short β-strands (yellow) are present in pUL25 N-terminal 1–160 aa. (f, g) The *in situ* (full-length) cryoEM structure and schematic model of the upper pUL25 (f) and lower pUL25 (g) segmented from the PRV map, with each consisting of an N-terminal loop (1–40 aa), a long helix (H2) and a hypothetical path of the unresolved loop (110–124 aa), and the C-terminal globular domain. The green asterisks mark the location of 124aa in pUL25.

identification of two bulky aromatic side-chains (a histidine and a tyrosine in Fig. 2d) of α-helix 1 (H1, aa 475–497) of the upper pUL25 that were visible in our density map (Fig. 2c, d). These refined structures provided the direct evidence for our reassignment of this density from pUL36, as previously suggested [45], to a second copy of pUL25 [45]. The H1 α-helix, which inserts into an interaction pocket present in the lower pUL25 subunit, may facilitate pUL25 homodimerization (Fig. 2c). The interface between the two atomic models of HSV-1 pUL25 fitted into the intertwining globular densities have complementary charge properties, suggesting that pUL25 dimerization might be driven by

electrostatic interactions (Fig. S2). As no regions of the two intertwining globular cryoEM densities were unaccounted for, we conclude that the pUL25 dimer is the only component of the CATC heads.

In addition to the head domain, pUL25 contains an N-terminal domain that mediates binding to the capsid surface [48], but was not included in the crystallography study [47]. The secondary structure prediction indicates that this segment contains an N-terminal extension (aa 1–40), a long α-helix (aa 41–109) and a loop (aa 110–124) connecting to the globular head domain (aa 125–598) (Fig. 2e). Among the five α-stem helices in the coiled-coil helix bundle, the two

longest are similar in shape and each is connected to a short tail (Fig. 2b). The lengths of the upper long-stem α-helix and its short tail match those predicted for the long α-helix and the N-terminal extension of pUL25, respectively (Fig. 2f, g). Therefore, we tentatively assigned the long stem α-helix on the top of the coiled-coil α-helix bundle, together with its short tail, to the N-terminal region of the upper pUL25 subunit, and the other long stem α-helix, together with its short tail, to the corresponding segment of the lower pUL25 subunit. While the stem α-helix of the lower pUL25 subunit was 20 Å longer than that of the upper pUL25 subunit, it was 15 Å closer to the corresponding globular head domain (Fig. 2f, g). Consequently, we speculate that part of the sequence between aa 110–124 contributes to the formation of the elongated stem α-helix of the lower pUL25 subunit. The N-terminal extensions of both the upper and lower pUL25 subunits that span the top of the V-shaped density drape over the two triplexes (Fig. 2a), which is consistent with a previous study that showed the pUL25 N-terminal domain extends to the triplex-binding region [43].

Structure of pUL17 and the assignment of the pUL36 stem α-helices

The V-shaped structure on the opposing end of the CATC coiled-coil helix bundle splay over the Ta and Tc capsid triplexes (Fig. 3a, b and Movie S3). The V-shaped density is formed by a monomer of pUL17 [45]. The mean density of the pUL17 structure was 92 % of that of the capsid and was much higher than that of the globular head densities, suggesting that pUL17 is more rigidly anchored on the capsid surface than pUL25.

The four α-helices predicted from the pUL17 sequence to be longer than 20 Å (H1-4) (Figs 3c and S3) were mapped onto the α-helices visualized in the CATC V-shaped density from the cryoEM reconstruction. Three long α-helices were observed in the V-shaped density, while the shortest of the five stem α-helices in the coiled-coil α-helix bundle was connected to the V-shaped density (Fig. 3d). This short α-helix may represent the fourth pUL17 helix. Among the three helices observed in the V-shaped density, the one located at the bottom of the Tc-binding domain contained a kink along its length. Since kinks in α-helices are typically created by proline residues, and only H2 contained a proline, we assigned H2 to the kinked α-helix in the Tc-binding domain (Fig. 3d). H1 was assigned to the α-helix connected to, and roughly parallel with, H2 in the V-shaped density, based on their proximity in space (Fig. 3e, f). We then assigned H4 (aa 199–215) to the stem α-helix, as, unlike H3, it was predicted to contain a coiled-coil by the *COILS* algorithm [49] (Fig. S4). Indeed, H4 is an amphipathic α-helix, with one side lined with hydrophobic side-chains that can interact with the other α-helixes in the bundle (Fig. 3e). Thus, H4 was assigned to the shortest stem helix in the coiled-coil α-helix bundle, and by elimination, H3 was assigned to the remaining α-helix.

Among the five stem helices in the coiled-coil helix bundle, one is assigned to pUL17 and two are assigned to the pUL25

homodimer. The remaining two medium-length stem α-helices have a similar shape and length (Fig. 3f). We hypothesize that these α-helices belong to the C-terminal capsid-binding domain of pUL36, which interacts with pUL25 [50, 51] at a stoichiometry of approximately 1 : 1 [52].

Comparing the PRV and KSHV capsid–tegument interface

Similar to the PRV CATC, the KSHV CATC contains a V-shaped density, a coiled-coil α-helix bundle and a globular head. However, only one pORF19 head density was visible in the KSHV reconstruction, which is in contrast to the pUL25 homodimer observed in PRV [53]. In addition, the location of the stem α-helix of pORF19 corresponded to the stem α-helix of the upper pUL25 subunit in PRV. Nevertheless, a second stem α-helix with a similar length, shape and location to the stem α-helix of the lower pUL25 in PRV, was observed in the α-helix bundle of the KSHV CATC (Fig. S5). This suggests that, similar to PRV pUL25, two copies of pORF19 are present in each CATC of KSHV, although the head domain of one of the two is not visible in the cryoEM reconstruction. Our inability to visualize the second pORF19 globular head means that it is either more flexible than its pUL25 counterpart in PRV, or that it is proteolytically removed from the KSHV capsid during assembly. Thus, we assigned the previously identified pORF19 subunit [53] as 'upper pORF19' and the other one as the 'lower pORF19', with the head domain of the latter not being visible in the KSHV density map. The relative density ratio between the stem α-helices of the upper and lower pUL25 subunits and the PRV capsid was 69 and 74 %, respectively. Assuming that this ratio reflects the relative occupancy of the pUL25 binding sites on the capsid (110 per capsid, excluding the unique portal-containing vertex), we estimate that there are 85 copies of pUL25 per PRV and 48 copies of pORF19 subunits per KSHV. The relative density of the two PRV pUL25 heads is 63 %, which is lower than that for their corresponding stem α-helices and indicates that there is some flexibility in head positioning on the capsid surface. The densities of the PRV pUL25 heads is much higher than the 27 % relative density of the single visible KSHV pORF19 head. Therefore, in addition to having lower occupancy, the pORF19 head domain in KSHV is more flexible than the corresponding pair of head domains in PRV. Finally, the stem α-helix of the upper pORF19 subunit in KSHV is 15 Å shorter and rotated 20° relative to the stem α-helix of the upper pUL25 subunit in PRV (Fig. 4a).

Consistent with a previous report of the lower pUL25 subunit interacting with two major capsid protein (MCP) subunits of the penton [45], we found that the upper pUL25 subunit also interacted with two penton MCP subunits (Fig. 4b and Movie. S1). Unlike KSHV, the PRV penton MCP subunits lacked the small capsid protein (SCP; VP26) (Fig. 4c, e and Movie. S1). KSHV juxtaposes the SCP and upper pORF19 head to opposing sides of the penton MCP [53] (Fig. 4d, f). The KSHV configuration produces a 5 nm
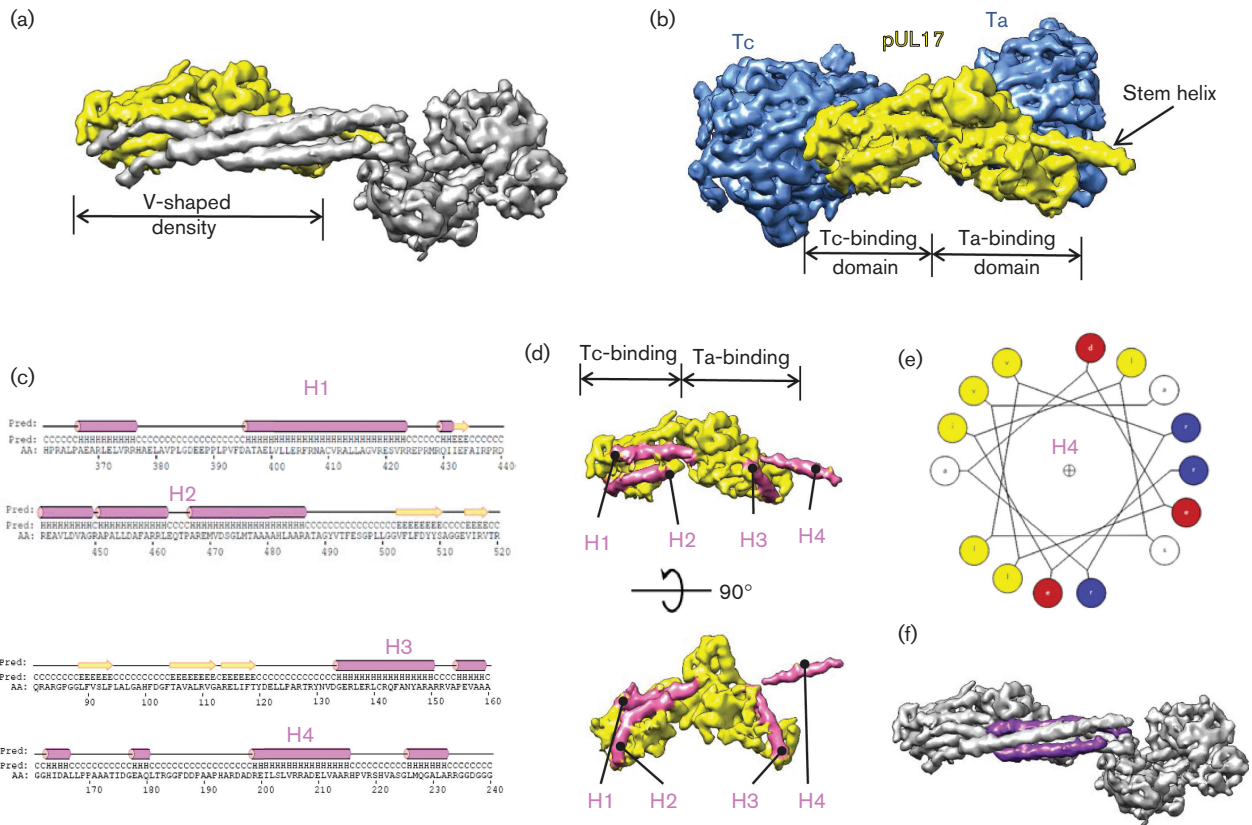
Fig. 3. Structure of pUL17 and the assignment of the pUL36 stem α-helices. (a) CATC structure of PRV with the pUL17 density shown in yellow. (b) pUL17 bridges two triplexes, Ta and Tc. The pUL17 are coloured yellow and the triplexes are coloured in light blue. The pUL17 density contains the V-shaped density and a stem helix. The V-shaped density can be divided into Ta and Tc binding domains. (c) All four α-helices (H1-4) that are longer than 20 Å, as identified from the secondary structural prediction of pUL17. (d) Two different views of pUL17 density. Of the four helices (H1-4, coloured pink) found in the map, three (H1–H4) are located in the V-shaped density. (e) Helix wheel diagram of H4 helix. Yellow, red and blue circles represent amino acids with large hydrophobic, negatively charged and positively charged side-chains, respectively. The white circles are amino acids with small hydrophobic (alanine) and polar uncharged (serine) side-chains. (f) CATC structure with the same orientation as in (a). Two helices of pUL36 are highlighted in purple.

displacement and an 80° rotation of the pORF19 head domain relative to the corresponding upper pUL25 head domain in PRV (Fig. 4a, e, f).

In addition to the two penton MCP contacts made by pUL25, pUL17 interacts with two adjacent MCP subunits in a peripentonal hexon (Fig. 5a, c and Movie S3). When rotated 60° around the channel axis of this hexon, one interaction site matches the other, indicating that the two interaction sites are located at equivalent positions on the two hexon MCP subunits (Fig. 5a, c and Movie S3). Each interaction site is on an extended hairpin structure (β-strand/loop/β-strand motif), as inferred from the corresponding location within the HSV-1 MCP upper domain structure (PDB ID: 1NO7) [46] and from the secondary structure prediction of the corresponding sequence of the MCP in PRV (Fig. 5c, e and Movie S3). Residues Gln545, Val546 and Arg547 of the MCP hairpin structure are closest to the pUL17 density at both binding sites, and thus may contribute to the interaction between MCP and pUL17. Unlike

PRV pUL17, which binds to two copies of MCP in the hexon, KSHV pORF32 (a homologue of PRV pUL17) only interacts with one MCP hexon subunit (Fig. 5b, d). Moreover, pUL17 bends 40° relative to pORF32 (Fig. 5f). KSHV pORF32 lacks the short stem helix of PRV pUL17 that is integrated into the coiled-coil helix bundle. Therefore, each coiled-coil α-helix bundle in the KSHV CATC only contains four α-helices instead of the five α-helices present in the PRV CATC.

DISCUSSION

Although CATC is not integral to the α-herpesvirus capsid structure, it is essential for stable genome encapsidation and the egress of capsids from the nucleus to the cytoplasm [28, 41, 54–57]. CATC also serves as the site of tegument attachment at the capsid vertices [50, 51, 58, 59]. Understanding how CATC performs and coordinates these critical functions requires a high-resolution map of its structure. In this report, we provide a 4.9 Å cryoEM reconstruction of the
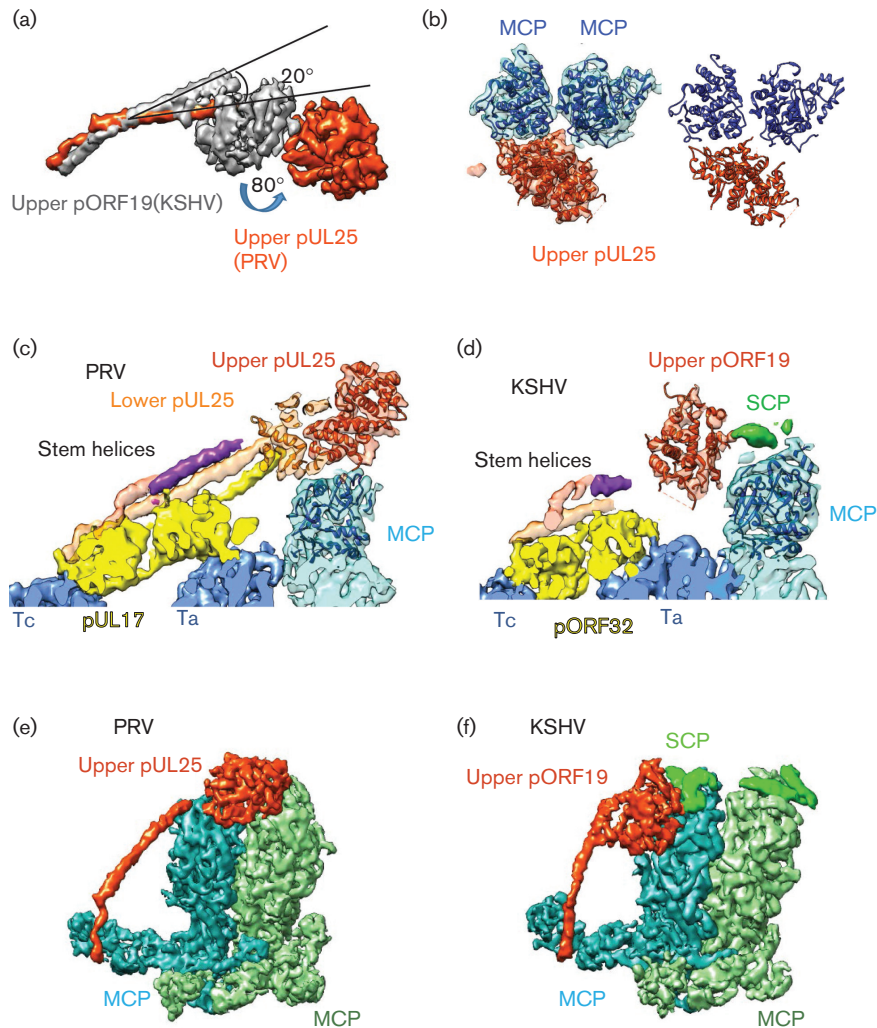
Fig. 4. Comparison of CATC interactions with penton in PRV and KSHV. (a) When the fivefold axes of the PRV and KSHV maps are aligned, the N-terminal helix is both longer and 20° further bent for the PRV pUL25 (orange) subunit in PRV compared to its KSHV homologue, the pORF19 (semi-transparent grey). The density of the pUL25 globular domain rotated 80° further than that of the pORF19. (b) The upper pUL25 interacts with two MCP subunits on penton. The HSV-1 pUL25 and two atomic models of the MCP upper domain (PDB ID: 1NO7) [46] are coloured red and blue, respectively. The density of the pUL25 and MCP is displayed in transparent red and blue, respectively, in the left figure. (c, d) The slabs of density at the same positions of PRV (a) and KSHV (b). The atomic models (ribbons) of HSV-1 pUL25 and MCPud were fitted into the density maps. KSHV contains the smallest capsid protein SCP (green) at the corresponding location of the upper pUL25 subunit. (e, f) Side views of the upper pUL25 and pORF19 interacting with penton capsid proteins in PRV (e) and KSHV (f), respectively.

PRV capsid from intact virions. The results provide the highest resolution yet obtained for a herpesvirus capsid, reveal a conserved architecture for CATC between PRV and KSHV, and rectify the precise contribution of the pUL36 tegument protein to the CATC structure.

Our results demonstrate that in the α-herpesvirus PRV, pUL17 and pUL25 interact with two hexon and two penton MCPs, respectively. Coupled with the homodimerization of pUL25, the surface area of interaction between the CATC and the capsid is more extensive than that observed in the γ-herpesvirus KSHV. In KSHV, the shorter stem α-helix of

pORF19, combined with steric hindrance from penton-associated SCP, likely liberates the lower pORF19 head domain from the MCP (Fig. 6), thereby preventing its observation by cryoEM [31].

The importance of the pUL25–capsid interaction during herpesvirus infection is underscored by the fact that pUL25 is essential for the egress of newly assembled C-capsids from the nucleus [54]. In addition, pUL25 is critical for viral genome encapsidation and it has been proposed that pUL25 stabilizes the capsid against the internal pressures exerted by the packaged genome [41, 60]. Although C-capsids have been observed

Fig. 5. Comparison of CATC interactions with hexon in PRV and KSHV. (a, b) Top view of a CATC and the CATC-interacting hexon in PRV (a) and KSHV (b). The hexon is shown in cyan, with light and heavy shades distinguishing the subunit boundaries. (c, d) Slice views of the boxed regions of (a, b) showing only two MCP subunits in CATC-interacting hexon in PRV (c) and KSHV (d). MCPud atomic models of HSV-1 are fitted in the map as ribbons. (e) The extended hairpin (β strand–loop–β strand motif) structure of the PRV MCP segment interacting with pUL17 as inferred from the fit HSV-1 MCPud model (left) and from the secondary structure prediction of the corresponding sequence of PRV MCP (right). (f) PRV pUL17 structure superimposed with its KSHV homologue (semi-transparent cyan), pORF32, revealing a 40° bend.

in the nucleus of cells infected by pUL25-null α-herpesviruses, they cannot be recovered following cell lysis [54, 60], suggesting that pUL25 is required for C-capsid stability. Furthermore, pUL25 mediates tegumentation through anchoring pUL36 to the capsid surface [32]. Notwithstanding these essential roles, a major roadblock to defining the molecular mechanisms underlying the multifunctionality of pUL25 has been the lack of an accurate understanding of the structure of pUL25 on the capsid surface.

Previously, the head domain of pUL25 was successfully crystallized and its structure determined by X-ray crystallography [47]. However, the absence of information regarding the location of pUL25 on the capsid surface, let alone its interactions with capsid proteins *in situ*, limited the utility of this structure for providing insights into how pUL25 contributes to the infectious cycle of the herpesviruses. The application of cryoEM enabled the visualization of the structure of pUL25 on the surface of PRV and HSV-1 capsids

Fig. 6. Schematic illustration of interactions of CATC in PRV (a) and KSHV (b). Two copies of pUL25 (pORF19) located on the capsid vertices in both PRV and KSHV. One of the pORF19 globular domains in KSHV that is not observed in the density map is shown in a fuzzy shape, and the other pORF19 binds one penton MCP. In PRV, the lack of SCP on the PRV penton and the longer N-terminal region of pUL25 seem to have enabled each pUL25 to bind two penton MCPs. The PRV pUL17 binds to two hexon MCP and it bends 40° compared to KSHV pORF32, which only binds to one hexon MCP.

[25, 43]. Both pUL25 and pUL17 are components of the previously described CATC, five copies of which radiate from each capsid vertex [26, 27]. Initial interpretations of cryoEM data erroneously placed pUL25 at the vertex-distal end of the CATC due to the intrinsic flexibility of pUL25, which reduced the resolution of the CATC complex to ~9 Å [43]. While recently obtained 7 Å structures have since correctly identified one of the two globular pUL25 densities in each CATC, the remaining globular density was misidentified as pUL36 [45]. This confusion likely resulted from the lower resolution obtained for this globular density in those reconstructions and the expectation that pUL36 would be present as an ordered density on the capsid surface [43, 45].

In this study, we used a direct electron detector in the super-resolution mode with electron counting and

improved the resolution of PRV to 4.9 Å. This improvement in resolution resulted in the visualization of numerous helices in the CATC, which matched the helices in the HSV-1 pUL25 crystal structure (PDB ID: 1NO7) [46]. From this high-resolution fitting, the globular domain previously assigned to pUL36 was clearly a second globular domain of pUL25 (Fig. 2c). The coiled-coil-forming N-terminal helix was also clearly resolved (Fig. 4f). The integration of our cryoEM structures and results from secondary structural prediction further allowed us to assign pUL17 and pUL36 in the CATC, and revealed their interactions with one another and with the surrounding capsid proteins. We hypothesize that the penton-associated pUL25 dimer provides a structural support that stabilizes the capsid against internal pressures exerted by the packaged genome [61]. We further note that the localization of the pUL25 dimer to

capsid pentons makes it readily accessible to interact with the nuclear egress complex and the tegument.

Intriguingly, the structural organization of the pUL25 dimer is reminiscent of those of several members of the kinesin superfamily of microtubule motor proteins [62, 63]. Kinesins typically consist of a cargo-binding coiled-coil tail domain and a dimeric globular motor domain that uses the energy generated by ATP hydrolysis to walk along microtubules [64]. In the absence of clear sequence homology between kinesins and pUL25, the similarity in their structural organization may be superficial. Even so, pUL25 has been reported to associate with and potentially bundle microtubules when expressed in the absence of other viral proteins [65]. Since many kinesins and microtubule-associated proteins promote microtubule bundling [66–68], these results suggest that pUL25 might contribute directly to intracellular microtubule-dependent α-herpesvirus capsid transport. Future efforts designed to test the functional significance of the pUL25-microtubule association should help test this exciting hypothesis.

METHODS

Virus isolation

Porcine kidney epithelial cells (PK15) were grown in eight 850 cm^2 roller bottles and infected with wild-type PRV (Becker strain, PRV-GS999) at a multiplicity of infection of 5. Supernatants were collected without disturbing adherent cells at 24 h post infection. Cell debris was cleared by 10 min of centrifugation at 4800 *g* at 4 °C. Supernatants were underlaid with 3 ml of a 10 % (w/v) Nycodenz solution in PBS in an SW28 centrifuge tube. Samples were centrifuged at 38500 *g* for 1 h at 4 °C. Viral pellets were resuspended in a total of 800 µl of PBS and shipped on wet ice for further processing. Virions were infectious and the titre of the concentrated stock was 6.0×10^{11} p.f.u. ml^{-1}.

CryoEM sample preparation and data collection

For cryoEM, 2.5 µL of purified PRV virion was applied to a glow-discharged Quantifoil R2/1 grid (EMS, Hatfield, PA, USA). The grid was blotted with filter paper to remove excess sample and flash-frozen in liquid ethane with a Vitrobot Mark IV (FEI, Hillsboro, OR, USA). The frozen hydrated grids were loaded into an FEI Titan Krios electron microscope operated at 300 kV for automated image acquisition with the data acquisition software Leginon [69]. Micrographs were acquired with a Gatan K2 Summit direct electron detection camera (Roper Technologies, Inc., Sarasota, FL, USA) operated in the super-resolution electron counting mode at a nominal magnification of 18 000× and defocus values ranging from −1.0 to −3.0 µm. The dose rate on the camera was set to~8 e$^-$/pixel/s and the total exposure time was 10 s fractionated into 40 frames of images with 0.25 s exposure time for each frame. Frame images were 1.6x binned using the Fourier cropping method, yielding a pixel size of 1.29 Å. The binned frame images were then aligned and averaged for correction of beam-induced drift

using the GPU-accelerated motion correction program [70]. The average images from all frames were used for defocus determination and particle picking, and those from frames 2–25 (corresponding to~18 e$^-$/Å^2 total dose on sample) were used for 3D reconstruction and refinement.

Image processing and data analysis

A total of 13 537 particles (1024×1024 pixels) were hand-picked from 1830 micrographs. The defocus values of these micrographs were determined by CTFFIND3 [71] and the selected particles were processed with the contrast transfer function by phase-flipping with the corresponding defocus and astigmatism values using Bsoft [72]. The particles were initially processed using EMAN [73] for an initial 3D reconstruction and refinement enforced with an icosahedral symmetry. The preliminary 3D map was then low-pass filtered to 60 Å to serve as a starting model and the particles were scaled to a pixel size of 1.61 Å for 3D auto-refinement by RELION [74] using the icosahedral symmetry. The final resolution was estimated with two independently refined maps from the halves of data set with the gold-standard FSC at the 0.143 criterion using the *relion_postprocess* program in RELION [75]. The local resolution was estimated by ResMap [76]. The cryoEM map was sharpened by B-factor and low-pass filtered to the stated resolution using the *relion_postprocess* program.

In order to better identify α-helices in the tegument densities, the map was filtered to 5.5 Å resolution with the cosine edge filter using *bfactor* [77] (http://grigorefflab.janelia.org/grigorieff/download_b.html) and then normalized by *e2proc3d.py* in EMAN2 [78]. The cryoEM densities of varies of the structures were segmented by 'volume tracer' and 'color zone' using UCSF Chimera [79]. Finally, the atomic model or density map was fitted with a corresponding density map by the 'Fit in Map' tool in Chimera.

To find the amino acids in PRV pUL25 that correspond to the HSV-1 pUL25 model, the online server SIM [80] was used for the protein sequence alignment between pUL25 in PRV and HSV. Secondary structure predictions for pUL25 and pUL17 were performed with JPred [81].

The atomic model of the α-helix H1 was built using COOT [82] from the density map for the upper pUL25 promoter filtered to 4.8 Å using *bfactor*. The electrostatic surface of the pUL25 dimer was calculated with the adaptive Poisson–Boltzmann solver [83]. Coiled-coil prediction was performed using *COILS* [49].

To measure the relative density ratio of the CATC subunits, the densities of the upper and lower pUL25 stem helixes and globular domains, pUL17 and the upper domain of the MCP were first segmented in the unsharpened EM map with a contour level equivalent to 0.3 Å^3/Dalton. Then the mean density of the protein densities was quantified by calculating the averaged density in the segmented region and subtracting the background density (i.e. the averaged density value of the region outside the capsid). The mean protein densities of pUL25 or pUL17 divided by that of the

upper domain of the hexon MCP are defined as relative density. The copy number of the protein is the relative density ratio multiplied by 60, which is the number of asymmetric units of an icosahedral symmetry.

Conflicts of interest

The authors declare that there are no conflicts of interest.

References

1. **Zerboni L, Sen N, Oliver SL, Arvin AM.** Molecular mechanisms of varicella zoster virus pathogenesis. *Nat Rev Microbiol* 2014;12:197–210.

2. **Pomeranz LE, Reynolds AE, Hengartner CJ.** Molecular biology of pseudorabies virus: impact on neurovirology and veterinary medicine. *Microbiol Mol Biol Rev* 2005;69:462–500.

3. **Kramer T, Enquist LW.** Directional spread of alphaherpesviruses in the nervous system. *Viruses* 2013;5:678–707.

4. **Smith G.** Herpesvirus transport to the nervous system and back again. *Annu Rev Microbiol* 2012;66:153–176.

5. **Antinone SE, Smith GA.** Retrograde axon transport of herpes simplex virus and pseudorabies virus: a live-cell comparative analysis. *J Virol* 2010;84:1504–1512.

6. **Markus A, Grigoryan S, Sloutskin A, Yee MB, Zhu H** *et al.* Varicella-zoster virus (VZV) infection of neurons derived from human embryonic stem cells: direct demonstration of axonal infection, transport of VZV, and productive neuronal infection. *J Virol* 2011;85:6220–6233.

7. **Lee JI, Sollars PJ, Baver SB, Pickard GE, Leelawong M** *et al.* A herpesvirus encoded deubiquitinase is a novel neuroinvasive determinant. *PLoS Pathog* 2009;5:e1000387.

8. **Smith BN, Banfield BW, Smeraski CA, Wilcox CL, Dudek FE** *et al.* Pseudorabies virus expressing enhanced green fluorescent protein: A tool for *in vitro* electrophysiological analysis of transsynaptically labeled neurons in identified central nervous system circuits. *Proc Natl Acad Sci USA* 2000;97:9264–9269.

9. **Zermann DH, Ishigooka M, Doggweiler R, Schubert J, Schmidt RA.** Central nervous system neurons labeled following the injection of pseudorabies virus into the rat prostate gland. *Prostate* 2000;44:240–247.

10. **Liu F, Zhou ZH.** Comparative virion structures of human herpesviruses. In: Arvin A, Campadelli-Fiume G, Mocarski E, Moore PS, Roizman B *et al.* (editors). *Human Herpesviruses: Biology, Therapy, and Immunoprophylaxis*. Cambridge: Cambridge University Press; 2007.

11. **Grünewald K, Desai P, Winkler DC, Heymann JB, Belnap DM** *et al.* Three-dimensional structure of herpes simplex virus from cryo-electron tomography. *Science* 2003;302:1396–1398.

12. **Dai W, Jia Q, Bortz E, Shah S, Liu J** *et al.* Unique structures in a tumor herpesvirus revealed by cryo-electron tomography and microscopy. *J Struct Biol* 2008;161:428–438.

13. **Mettenleiter TC, Klupp BG, Granzow H.** Herpesvirus assembly: an update. *Virus Res* 2009;143:222–234.

14. **Wolfstein A, Nagel CH, Radtke K, Döhner K, Allan VJ** *et al.* The inner tegument promotes herpes simplex virus capsid motility along microtubules *in vitro*. *Traffic* 2006;7:227–237.

15. **Luxton GW, Haverlock S, Coller KE, Antinone SE, Pincetic A** *et al.* Targeting of herpesvirus capsid transport in axons is coupled to association with specific sets of tegument proteins. *Proc Natl Acad Sci USA* 2005;102:5832–5837.

16. **Granzow H, Klupp BG, Mettenleiter TC.** Entry of pseudorabies virus: an immunogold-labeling study. *J Virol* 2005;79:3200–3205.

17. **Zaichick SV, Bohannon KP, Hughes A, Sollars PJ, Pickard GE** *et al.* The herpesvirus VP1/2 protein is an effector of dynein-mediated capsid transport and neuroinvasion. *Cell Host Microbe* 2013; 13:193–203.

18. **Schipke J, Pohlmann A, Diestel R, Binz A, Rudolph K** *et al.* The C terminus of the large tegument protein pUL36 contains multiple capsid binding sites that function differently during assembly and cell entry of herpes simplex virus. *J Virol* 2012;86:3682–3700.

19. **Abaitua F, Hollinshead M, Bolstad M, Crump CM, O'Hare P.** A nuclear localization signal in herpesvirus protein VP1-2 is essential for infection via capsid routing to the nuclear pore. *J Virol* 2012;86:8998–9014.

20. **Roberts AP, Abaitua F, O'Hare P, Mcnab D, Rixon FJ** *et al.* Differing roles of inner tegument proteins pUL36 and pUL37 during entry of herpes simplex virus type 1. *J Virol* 2009;83:105–116.

21. **Huffmaster NJ, Sollars PJ, Richards AL, Pickard GE, Smith GA.** Dynamic ubiquitination drives herpesvirus neuroinvasion. *Proc Natl Acad Sci USA* 2015;112:12818–12823.

22. **Krautwald M, Fuchs W, Klupp BG, Mettenleiter TC.** Translocation of incoming pseudorabies virus capsids to the cell nucleus is delayed in the absence of tegument protein pUL37. *J Virol* 2009; 83:3389–3396.

23. **Mcelwee M, Beilstein F, Labetoulle M, Rixon FJ, Pasdeloup D.** Dystonin/BPAG1 promotes plus-end-directed transport of herpes simplex virus 1 capsids on microtubules during entry. *J Virol* 2013;87:11008–11018.

24. **Jovasevic V, Liang L, Roizman B.** Proteolytic cleavage of VP1-2 is required for release of herpes simplex virus 1 DNA into the nucleus. *J Virol* 2008;82:3311–3319.

25. **Zhou ZH, Chen DH, Jakana J, Rixon FJ, Chiu W.** Visualization of tegument-capsid interactions and DNA in intact herpes simplex virus type 1 virions. *J Virol* 1999;73:3210–3218.

26. **Toropova K, Huffman JB, Homa FL, Conway JF.** The herpes simplex virus 1 UL17 protein is the second constituent of the capsid vertex-specific component required for DNA packaging and retention. *J Virol* 2011;85:7513–7522.

27. **Conway JF, Cockrell SK, Copeland AM, Newcomb WW, Brown JC** *et al.* Labeling and localization of the herpes simplex virus capsid protein UL25 and its interaction with the two triplexes closest to the penton. *J Mol Biol* 2010;397:575–586.

28. **Leelawong M, Lee JI, Smith GA.** Nuclear egress of pseudorabies virus capsids is enhanced by a subspecies of the large tegument protein that is lost upon cytoplasmic maturation. *J Virol* 2012;86: 6303–6314.

29. **Fan WH, Roberts AP, Mcelwee M, Bhella D, Rixon FJ** *et al.* The large tegument protein pUL36 is essential for formation of the capsid vertex-specific component at the capsid-tegument interface of herpes simplex virus 1. *J Virol* 2015;89:1502–1511.

30. **Trus BL, Newcomb WW, Cheng N, Cardone G, Marekov L** *et al.* Allosteric signaling and a nuclear exit strategy: binding of UL25/UL17 heterodimers to DNA-Filled HSV-1 capsids. *Mol Cell* 2007; 26:479–489.

31. **Dai X, Gong D, Wu TT, Sun R, Zhou ZH.** Organization of capsid-associated tegument components in kaposi's sarcoma-associated herpesvirus. *J Virol* 2014;88:12694–12702.

32. **Salmon B, Cunningham C, Davison AJ, Harris WJ, Baines JD.** The herpes simplex virus type 1 U(L)17 gene encodes virion tegument proteins that are required for cleavage and packaging of viral DNA. *J Virol* 1998;72:3779–3788.

33. **Tomishima MJ, Enquist LW.** A conserved alpha-herpesvirus protein necessary for axonal localization of viral membrane proteins. *J Cell Biol* 2001;154:741–752.

34. **Parsons LR, Tafuri YR, Shreve JT, Bowen CD, Shipley MM** *et al.* Rapid genome assembly and comparison decode intrastrain variation in human alphaherpesviruses. *mBio* 2015;6:2.

35. **Tombácz D, Sharon D, Oláh P, Csabai Z, Snyder M** *et al.* Strain Kaplan of pseudorabies virus Genome sequenced by PacBio Single-Molecule Real-Time sequencing technology. *Genome Announc* 2014;2:e00628-14.

36. **Yu X, Shah S, Lee M, Dai W, Lo P** *et al.* Biochemical and structural characterization of the capsid-bound tegument proteins of human cytomegalovirus. *J Struct Biol* 2011;174:451–460.

37. **Dai X, Yu X, Gong H, Jiang X, Abenes G** *et al.* The smallest capsid protein mediates binding of the essential tegument protein pp150 to stabilize DNA-containing capsids in human cytomegalovirus. *PLoS Pathog* 2013;9:e1003525.

38. **Chen DH, Jiang H, Lee M, Liu F, Zhou ZH.** Three-dimensional visualization of tegument/capsid interactions in the intact human cytomegalovirus. *Virology* 1999;260:10–16.

39. **Trus BL, Gibson W, Cheng N, Steven AC.** Capsid structure of simian cytomegalovirus from cryoelectron microscopy: evidence for tegument attachment sites. *J Virol* 1999;73:2181–2192.

40. **Yu X, Jih J, Jiang J, Zhou ZH.** Atomic structure of the human cytomegalovirus capsid with its securing tegument layer of pp150. *Science* 2017;356:6345.

41. **McNab AR, Desai P, Person S, Roof LL, Thomsen DR** *et al.* The product of the herpes simplex virus type 1 UL25 gene is required for encapsidation but not for cleavage of replicated viral DNA. *J Virol* 1998;72:1060–1070.

42. **Meyer HH, Ripalti A, Landini MP, Radsak K, Kern HF** *et al.* Human cytomegalovirus late-phase maturation is blocked by stably expressed UL32 antisense mRNA in astrocytoma cells. *J Gen Virol* 1997;78:2621–2631.

43. **Homa FL, Huffman JB, Toropova K, Lopez HR, Makhov AM** *et al.* Structure of the pseudorabies virus capsid: comparison with herpes simplex virus type 1 and differential binding of essential minor proteins. *J Mol Biol* 2013;425:3415–3428.

44. **Cockrell SK, Huffman JB, Toropova K, Conway JF, Homa FL.** Residues of the UL25 protein of herpes simplex virus that are required for its stable interaction with capsids. *J Virol* 2011;85:4875–4887.

45. **Huet A, Makhov AM, Huffman JB, Vos M, Homa FL** *et al.* Extensive subunit contacts underpin herpesvirus capsid stability and interior-to-exterior allostery. *Nat Struct Mol Biol* 2016;23:531–539.

46. **Bowman BR, Baker ML, Rixon FJ, Chiu W, Quiocho FA.** Structure of the herpesvirus major capsid protein. *Embo J* 2003;22:757–765.

47. **Bowman BR, Welschhans RL, Jayaram H, Stow ND, Preston VG** *et al.* Structural characterization of the UL25 DNA-packaging protein from herpes simplex virus type 1. *J Virol* 2006;80:2309–2317.

48. **Cockrell SK, Sanchez ME, Erazo A, Homa FL.** Role of the UL25 protein in herpes simplex virus DNA encapsidation. *J Virol* 2009;83:47–57.

49. **Lupas A, van Dyke M, Stock J.** Predicting coiled coils from protein sequences. *Science* 1991;252:1162–1164.

50. **Coller KE, Lee JI, Ueda A, Smith GA.** The capsid and tegument of the alphaherpesviruses are linked by an interaction between the UL25 and VP1/2 proteins. *J Virol* 2007;81:11790–11797.

51. **Pasdeloup D, Blondel D, Isidro AL, Rixon FJ.** Herpesvirus capsid association with the nuclear pore complex and viral DNA release involve the nucleoporin CAN/Nup214 and the capsid protein pUL25. *J Virol* 2009;83:6610–6623.

52. **Bohannon KP, Jun Y, Gross SP, Smith GA.** Differential protein partitioning within the herpesvirus tegument and envelope underlies a complex and variable virion architecture. *Proc Natl Acad Sci USA* 2013;110:E1613–E1620.

53. **Dai X, Gong D, Xiao Y, Wu TT, Sun R** *et al.* CryoEM and mutagenesis reveal that the smallest capsid protein cements and stabilizes Kaposi's sarcoma-associated herpesvirus capsid. *Proc Natl Acad Sci USA* 2015;112:E649–E656.

54. **Klupp BG, Granzow H, Keil GM, Mettenleiter TC.** The capsid-associated UL25 protein of the alphaherpesvirus pseudorabies virus is nonessential for cleavage and encapsidation of genomic DNA but is required for nuclear egress of capsids. *J Virol* 2006;80:6235–6246.

55. **Leelawong M, Guo D, Smith GA.** A physical link between the pseudorabies virus capsid and the nuclear egress complex. *J Virol* 2011;85:11675–11684.

56. **Kuhn J, Leege T, Klupp BG, Granzow H, Fuchs W** *et al.* Partial functional complementation of a pseudorabies virus UL25 deletion mutant by herpes simplex virus 1 pUL25 indicates overlapping functions of alphaherpesvirus pUL25 proteins. *J Virol* 2008; 82:5725–5734.

57. **Luxton GW, Lee JI, Haverlock-Moyns S, Schober JM, Smith GA.** The pseudorabies virus VP1/2 tegument protein is required for intracellular capsid transport. *J Virol* 2006;80:201–209.

58. **Cardone G, Newcomb WW, Cheng N, Wingfield PT, Trus BL** *et al.* The UL36 tegument protein of herpes simplex virus 1 has a composite binding site at the capsid vertices. *J Virol* 2012;86:4058–4064.

59. **Uetz P, Dong YA, Zeretzke C, Atzler C, Baiker A** *et al.* Herpesviral protein networks and their interaction with the human proteome. *Science* 2006;311:239–242.

60. **Stow ND.** Packaging of genomic and amplicon DNA by the herpes simplex virus type 1 UL25-null mutant KUL25NS. *J Virol* 2001;75: 10755–10765.

61. **Bauer DW, Huffman JB, Homa FL, Evilevitch A.** Herpes virus genome, the pressure is on. *J Am Chem Soc* 2013;135:11216–11221.

62. **Woehlke G, Schliwa M.** Walking on two heads: the many talents of kinesin. *Nat Rev Mol Cell Biol* 2000;1:50–58.

63. **Hirokawa N, Pfister KK, Yorifuji H, Wagner MC, Brady ST** *et al.* Submolecular domains of bovine brain kinesin identified by electron microscopy and monoclonal antibody decoration. *Cell* 1989; 56:867–878.

64. **Kull FJ, Sablin EP, Lau R, Fletterick RJ, Vale RD.** Crystal structure of the kinesin motor domain reveals a structural similarity to myosin. *Nature* 1996;380:550–555.

65. **Kaelin K, Dezélée S, Masse MJ, Bras F, Flamand A.** The UL25 protein of pseudorabies virus associates with capsids and localizes to the nucleus and to microtubules. *J Virol* 2000;74: 474–482.

66. **MacRae TH.** Microtubule organization by cross-linking and bundling proteins. *Biochim Biophys Acta* 1992;1160:145–155.

67. **Straube A, Hause G, Fink G, Steinberg G.** Conventional kinesin mediates microtubule-microtubule interactions *in vivo*. *Mol Biol Cell* 2006;17:907–916.

68. **Andrews SB, Gallant PE, Leapman RD, Schnapp BJ, Reese TS.** Single kinesin molecules crossbridge microtubules *in vitro*. *Proc Natl Acad Sci USA* 1993;90:6503–6507.

69. **Suloway C, Pulokas J, Fellmann D, Cheng A, Guerra F** *et al.* Automated molecular microscopy: the new Leginon system. *J Struct Biol* 2005;151:41–60.

70. **Li X, Mooney P, Zheng S, Booth CR, Braunfeld MB** *et al.* Electron counting and beam-induced motion correction enable near-atomic-resolution single-particle cryo-EM. *Nat Methods* 2013;10: 584–590.

71. **Mindell JA, Grigorieff N.** Accurate determination of local defocus and specimen tilt in electron microscopy. *J Struct Biol* 2003;142: 334–347.

72. **Heymann JB, Belnap DM.** Bsoft: image processing and molecular modeling for electron microscopy. *J Struct Biol* 2007;157: 3–18.

73. **Ludtke SJ, Baldwin PR, Chiu W.** EMAN: semiautomated software for high-resolution single-particle reconstructions. *J Struct Biol* 1999;128:82–97.

74. **Scheres SH.** RELION: implementation of a Bayesian approach to cryo-EM structure determination. *J Struct Biol* 2012;180:519–530.

75. **Scheres SH, Chen S.** Prevention of overfitting in cryo-EM structure determination. *Nat Methods* 2012;9:853–854.

76. **Kucukelbir A, Sigworth FJ, Tagare HD.** Quantifying the local resolution of cryo-EM density maps. *Nat Methods* 2014;11:63–65.

77. **Grigorieff N.** Three-dimensional structure of bovine NADH:ubiquinone oxidoreductase (complex I) at 22 A in ice. *J Mol Biol* 1998;277:1033–1046.

78. **Tang G, Peng L, Baldwin PR, Mann DS, Jiang W** *et al.* EMAN2: an extensible image processing suite for electron microscopy. *J Struct Biol* 2007;157:38–46.

79. **Pettersen EF, Goddard TD, Huang CC, Couch GS, Greenblatt DM** *et al.* UCSF Chimera - a visualization system for exploratory research and analysis. *J Comput Chem* 2004;25:1605–1612.

80. **Huang X, Miller W.** A time-efficient, linear-space local similarity algorithm. *Adv Appl Math* 1991;12:337–357.

81. **Drozdetskiy A, Cole C, Procter J, Barton GJ.** JPred4: a protein secondary structure prediction server. *Nucleic Acids Res* 2015;43:W389–W394.

82. **Emsley P, Cowtan K.** Coot: model-building tools for molecular graphics. *Acta Crystallogr D Biol Crystallogr* 2004;60:2126–2132.

83. **Baker NA, Sept D, Joseph S, Holst MJ, Mccammon JA.** Electrostatics of nanosystems: application to microtubules and the ribosome. *Proc Natl Acad Sci USA* 2001;98:10037–10041.